



Irregularity Index for Vector-Valued Morphological Operators

Marcos Valle, Marco Aurélio Granero, Samuel Francisco, Santiago Velasco-Forero

► To cite this version:

Marcos Valle, Marco Aurélio Granero, Samuel Francisco, Santiago Velasco-Forero. Irregularity Index for Vector-Valued Morphological Operators. *Journal of Mathematical Imaging and Vision*, 2022, 64 (7), pp.1-17. 10.1007/s10851-022-01092-0 . hal-03649895

HAL Id: hal-03649895

<https://hal.science/hal-03649895>

Submitted on 23 Apr 2022

HAL is a multi-disciplinary open access archive for the deposit and dissemination of scientific research documents, whether they are published or not. The documents may come from teaching and research institutions in France or abroad, or from public or private research centers.

L'archive ouverte pluridisciplinaire **HAL**, est destinée au dépôt et à la diffusion de documents scientifiques de niveau recherche, publiés ou non, émanant des établissements d'enseignement et de recherche français ou étrangers, des laboratoires publics ou privés.

Irregularity Index for Vector-Valued Morphological Operators

Marcos Eduardo Valle · Samuel Francisco · Marco
Aur lio Granero · Santiago Velasco-Forero

the date of receipt and acceptance should be inserted later

Abstract Mathematical morphology is a valuable theory of nonlinear operators widely used for image processing and analysis. Although initially conceived for binary images, mathematical morphology has been successfully extended to vector-valued images using several approaches. Vector-valued morphological operators based on total orders are particularly promising because they circumvent the problem of false colors. On the downside, they often introduce irregularities in the output image. This paper proposes measuring the irregularity of a vector-valued morphological operator by the relative gap between the generalized sum of pixel-wise distances and the Wasserstein metric. Apart from introducing a measure of the irregularity, referred to as the irregularity index, this paper also addresses its computational implementation. Precisely, we distinguish between the ideal global and the practical local irregularity indexes. The local irregularity index, which can be computed more quickly by aggregating values of local windows, yields a lower bound for the global irregularity index. Computational experiments with natural images illustrate the effectiveness of the proposed irregularity indexes.

Keywords mathematical morphology · vector-valued images · total order · irregularity issue · optimal transport.

1 Introduction

Mathematical morphology (MM) is a nonlinear theory that uses geometric and topological concepts for image and signal processing [18, 29]. The theory of mathematical morphology is usually defined on an algebraic structure called complete lattices, which is satisfactory

This work was supported in part by the S o Paulo Research Foundation (FAPESP) under grant no 2019/02278-2.

Marcos Eduardo Valle
Universidade Estadual de Campinas, Campinas – SP, Brazil. E-mail: valle@ime.unicamp.br

Samuel Francisco and Marco Aur lio Granero
Instituto Federal de Educa  o, Ci ncia e Tecnologia de S o Paulo, S o Paulo – SP, Brazil.

Santiago Velasco-Forero
Center of Mathematical Morphology, Mines ParisTech, PSL Research University, Paris, France

for binary and gray-scale images [14, 22]. In the case of vector-valued images, vector spaces endowed with a total order are one of the most comfortable frameworks for the extension of morphological processing [1, 2, 36]. Approaches that have been recently formulated using total orderings include [17, 24, 31, 33–35]. Despite their successful applications for color and hyperspectral image processing, Chevallier and Angulo showed that the information contained in a total order is too weak to reproduce the natural topology of the value space [6]. As a consequence, morphological operators may introduce irregularities and aliasing on images. Our motivation is to formulate measures to study the irregularity implied by a morphological operator on vector-valued images. We believe this is the first work proposing a framework based on the Wasserstein metric to score the irregularity effect considering pairs of input/output images besides our conference paper [30]. Indeed, this paper extends [30] by presenting more efficient estimators for the irregularity measure using local windows and entropic regularized optimal transport methods [19, 26]. This paper also presents extensive computational experiments to show the effectiveness of the proposed irregularity measures.

The paper is organized as follows: Section 2 reviews mathematical morphology concepts for vector-valued images and the difficulties produced by operators based on total orders. Sections 3 and 4 present our proposed irregularity measure. Additionally, results on natural images show the goodness of the proposed measure. The paper ends with Section 5 including conclusions and recommendations for future works.

2 Basic Concepts on Mathematical Morphology

Let us begin by presenting the basic concepts and the notations used in this paper. First, an image \mathbf{I} corresponds to a mapping from a point set D to a value set \mathbb{V} , that is, $\mathbf{I} : D \rightarrow \mathbb{V}$. The set of all images from a domain D to \mathbb{V} is denoted by $\mathcal{V} = \mathbb{V}^D$. Throughout the paper, the set D is finite with $N_D = \text{Card}(D)$ points. Moreover, we assume D is included in a space \mathcal{E} , where $(\mathcal{E}, +)$ is a group. Usually, we consider $\mathcal{E} = \mathbb{R}^2$ or $\mathcal{E} = \mathbb{Z}^2$ with the usual addition. We also assume the value set \mathbb{V} is a complete lattice equipped with a metric $d : \mathbb{V} \times \mathbb{V} \rightarrow [0, +\infty)$. For simplicity, we consider the RGB color space endowed with the Euclidean distance throughout the paper.

2.1 Mathematical Morphology on Complete Lattices

Mathematical morphology (MM) is mainly concerned with image operators used to extract relevant geometric and topological information from an image [7, 14, 18, 29]. The two elementary operators of MM are dilations and erosions. Many other operators, such as opening, closing, and the morphological gradient, are obtained by combining the elementary morphological operators.

Complete lattices provide an appropriate mathematical background for defining the elementary morphological operators [14, 22]. A complete lattice \mathbb{L} is a partially ordered set in which any subset $X \subset \mathbb{L}$ has both an infimum and a supremum [3]. The infimum and the supremum of X are denoted by $\bigwedge X$ and $\bigvee X$, respectively.

The elementary morphological operators are those that commute with the supremum and the infimum operations in a complete lattice. When the value set \mathbb{V} is a complete lattice, the operators $\delta_S, \varepsilon_S : \mathcal{V} \rightarrow \mathcal{V}$ given by the following equations are respectively a dilation

and an erosion:

$$\delta_S(\mathbf{I})(p) = \bigvee_{\substack{s \in S \\ p-s \in D}} \mathbf{I}(p-s) \quad \text{and} \quad \varepsilon_S(\mathbf{I})(p) = \bigwedge_{\substack{s \in S \\ p+s \in D}} \mathbf{I}(p+s), \quad (1)$$

where $S \subseteq \mathcal{E}$ is a finite set referred to as the structuring element (SE) [29]. The images $\delta_S(\mathbf{I})$ and $\varepsilon_S(\mathbf{I})$ are the dilation and the erosion of \mathbf{I} by the structuring element S , respectively. Although there exist more general definitions, the elementary morphological operators given by (1) are widely used in practical situations. Combining dilations and erosions, we obtain many other morphological operators. In this paper, we focus on elementary operators defined by (1). We also consider openings γ_S and closings ϕ_S , which are obtained by the compositions $\gamma_S = \delta_S \circ \varepsilon_S$ and $\phi_S = \varepsilon_S \circ \delta_S$ [29].

2.2 Vector-Valued Mathematical Morphology

Let us now address morphological operators for vector-valued images. A vector-valued image is obtained by considering $\mathbb{V} \subseteq \mathbb{R}^d$, where $\mathbb{R} = \mathbb{R} \cup \{-\infty, +\infty\}$ and $d \geq 2$. Vector-valued dilations and erosions can be defined using (1) whenever the vector-valued set \mathbb{V} is a complete lattice. However, there are several ordering schemes for vector-valued sets. Defining an appropriate ordering scheme is one of the main challenges of vector-valued MM. The following references address interesting directions of research on vector-valued MM [1, 2, 5, 6, 12, 17, 31, 33, 34, 36].

As examples of ordering schemes on vector-valued sets, let us recall the marginal and the lexicographical orderings [2]. The marginal ordering is defined as follows for all $\mathbf{u} = (u_1, \dots, u_d) \in \mathbb{V}$ and $\mathbf{v} = (v_1, \dots, v_d) \in \mathbb{V}$:

$$\mathbf{u} \leq_M \mathbf{v} \iff u_i \leq v_i, \forall i = 1, \dots, d, \quad (2)$$

where “ \leq ” denotes the usual ordering on \mathbb{R} . The marginal ordering is also known as the component-wise ordering or the Cartesian product ordering. The lexicographical ordering is defined as follows:

$$\mathbf{u} \leq_L \mathbf{v} \iff \exists i : u_i \leq v_i \text{ and } u_j = v_j, \forall j < i. \quad (3)$$

In contrast to the marginal ordering, the lexicographical ordering is a total ordering. Thus, at least one of the inequalities $\mathbf{u} \leq_L \mathbf{v}$ or $\mathbf{v} \leq_L \mathbf{u}$ holds for any $\mathbf{u}, \mathbf{v} \in \mathbb{V}$.

There are many other approaches to vector-valued mathematical morphology besides the marginal and lexicographical approaches. The following papers survey several interesting approaches [1, 2, 36]. For comparative purposes, in this paper, we consider two approaches based on reduced orderings [11], and one approach based on the Loewner order [5].

A reduced ordering is defined by a surjective mapping $\rho : \mathbb{V} \rightarrow \mathbb{L}$ that maps the value set to a complete lattice as follows:

$$\mathbf{u} \leq_\rho \mathbf{v} \iff \rho(\mathbf{u}) \leq_{\mathbb{L}} \rho(\mathbf{v}). \quad (4)$$

A reduced ordering is not a partial order but a preorder because it may fail to be antisymmetric; that is, the inequalities $\mathbf{u} \leq_\rho \mathbf{v}$ and $\mathbf{v} \leq_\rho \mathbf{u}$ do not necessarily imply $\mathbf{u} = \mathbf{v}$. Nevertheless, reduced orderings can be used for the development of effective vector-valued morphological operators [11]. Precisely, combining (4) with look-up tables (LUTs), one can define computationally efficient vector-valued morphological operators taking advantage of

gray-scale morphological operators [36]. Together with a LUT, a reduced ordering given by (4) becomes a total ordering on the set $V(\mathbf{I}) = \{\mathbf{I}(p) : p \in D\}$ of values of an image \mathbf{I} . Moreover, the surjective mapping $\rho : \mathbb{V} \rightarrow \mathbb{L}$ can be defined using machine learning techniques [36]. Accordingly, depending on how the mapping ρ is determined, a morphological approach can be classified as supervised or unsupervised. We consider a radial-basis function support vector machine (SVM) as a representative supervised vector-valued approach [34]. Also, the statistical projection depth function is considered as a representative example of an unsupervised reduced ordering-based approach [35]. These two vector-valued morphological approaches are briefly revised in Appendix A.

Besides the marginal approach, we consider in this paper a second vector-valued morphological approach based on a partial order for comparison purposes. Specifically, we consider the approach to color-morphology based on the Loewner order proposed by Burgeth and Kleefeld [5]. The Loewner order is a partial order on the set of symmetric matrices. Formally, given symmetric matrices A and B , the Loewner order is defined by

$$\mathbf{A} \leq_w \mathbf{B} \iff \mathbf{B} - \mathbf{A} \text{ is positive semidefinite.} \quad (5)$$

The Loewner order has been successfully applied for the development of vector-valued morphological approaches [4,5]. In particular, the Loewner order can be used as follows for defining morphological operators for color images. First, a color value is represented using hue (H), chroma (C), and luminance (L) instead of the traditional RGB representation [9, 16, 15, 10]. Geometrically, the considered HCL space corresponds to a bi-cone centered at zero, with tips at $(0, 0, 1)$ and $(0, 0, -1)$ and a circular base of radius one on the horizontal plane. Then, each coordinate of the bi-cone is mapped onto a symmetric 2×2 matrix \mathbf{A} such that

$$-\frac{1}{\sqrt{2}}\mathbf{I} \leq_w \mathbf{A} \leq_w \frac{1}{\sqrt{2}}\mathbf{I},$$

where \mathbf{I} denotes the identity matrix. Finally, the isomorphism between colors and symmetric 2×2 matrices allows defining the so-called Loewner approach for color morphology¹.

2.3 The False Colors Problem Versus the Irregularity Issue

One problem on vector-valued MM is the creation of “false colors” or, more generally, false values [28]. A morphological operator $\psi : \mathcal{V} \rightarrow \mathcal{V}$ introduces false values whenever there are values in $\psi(\mathbf{I})$ which do not belong to the original image \mathbf{I} . Formally, let $2^{\mathbb{V}}$ denote the power set of \mathbb{V} and let $V : \mathcal{V} \rightarrow 2^{\mathbb{V}}$ be the mapping given by

$$V(\mathbf{I}) = \{\mathbf{I}(p) : p \in D\}, \quad \forall \mathbf{I} \in \mathcal{V}. \quad (6)$$

A morphological operator ψ introduces false colors if the set difference $V(\psi(\mathbf{I})) \setminus V(\mathbf{I})$ is not empty. The abnormal false values can be a problem in some applications such as when dealing with satellite data [28]. Using a partial order such as the marginal or the Loewner orders, the dilation and the erosion given by (1) usually yield false colors.

A total order, such as the lexicographical order and a reduced ordering combined with a look-up table, circumvents the problem of false values [28]. Using a total order, the supremum and the infimum of a finite set are elements of the set, i.e., they coincide with the

¹ The source-codes for the Loewner morphological approach can be found at <https://www.math.tu-cottbus.de/INSTITUT/lsmwr/kleefeld/SourcePRL/>.

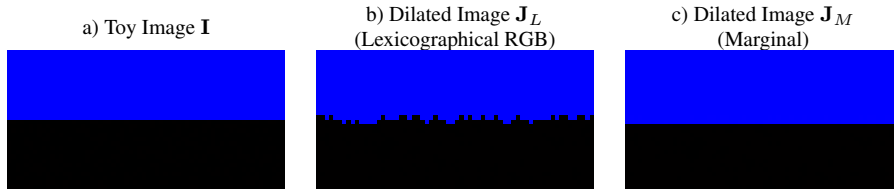


Fig. 1 Illustrative example of the irregularity issue. Image with three colors and its corresponding dilation by a cross structuring element using the RGB lexicographical and marginal orderings.

maximum and minimum operations, respectively. As a consequence, if D is finite, the elementary morphological operators given by (1) only contain values of the input image \mathbf{I} .

On the downside, a total order can be irregular in a metric space. According to Chevallier and Angulo, the irregularities follow because the topology induced by a total order may not reproduce the topology of a metric space [6]. Specifically, let the value set \mathbb{V} be a totally ordered set as well as a metric space, with metric $d : \mathbb{V} \times \mathbb{V} \rightarrow [0, +\infty)$. Chevallier and Angulo showed that there exist $\mathbf{u}, \mathbf{v}, \mathbf{w} \in \mathbb{V}$ such that $\mathbf{u} \leq \mathbf{v} \leq \mathbf{w}$ but $d(\mathbf{u}, \mathbf{w}) < d(\mathbf{u}, \mathbf{v})$ under mild conditions with respect to the connectivity of \mathbb{V} . In words, although \mathbf{u} is closer to \mathbf{w} than to \mathbf{v} , the inequalities $\mathbf{u} \leq \mathbf{v} \leq \mathbf{w}$ suggest \mathbf{w} is farther from \mathbf{u} than \mathbf{v} . Since the morphological operators are defined using the extrema operators, they do not take the metric of \mathbb{V} into account.

A visual interpretation of the irregularity is shown in Figure 1, which is very similar to an example provided in [6]. Figure 1a) shows an image with three RGB colors, namely $\mathbf{u} = (0, 0, 0)$, $\mathbf{v} = (0, 0, 1)$, and $\mathbf{w} = (1/255, 0, 0)$. The toy image \mathbf{I} is obtained by replacing pure black values \mathbf{u} by \mathbf{w} with probability 0.3 from an image of size 32×64 with two stripes of colors blue and black. The dilations $\mathbf{J}_L = \delta_S^L(\mathbf{I})$ and $\mathbf{J}_M = \delta_S^M(\mathbf{I})$ by a cross structuring element S obtained using the lexicographical RGB and the marginal ordering schemes are also depicted in Figure 1. Visually, \mathbf{u} and \mathbf{w} are black colors while \mathbf{v} is a pure blue. Using the Euclidean distance, we obtain $d(\mathbf{u}, \mathbf{v}) = 1$ and $d(\mathbf{u}, \mathbf{w}) = 0.005$. These distances agree with our color perception. However, using the lexicographical ordering, we obtain $\mathbf{u} \leq_L \mathbf{v} \leq_L \mathbf{w}$. As a consequence, the following happens when we compute the dilation $\delta_S^L(\mathbf{I}) = \mathbf{J}_L$ using the lexicographical ordering: the blue \mathbf{v} advances over the black \mathbf{u} but it is overlaid by the black \mathbf{w} , resulting in the irregularities shown in Figure 1b). In contrast, the dilated image depicted in Figure 1c) obtained using the marginal ordering does not present any visual irregularity.

Although we know that the irregularity results from a divergence between the topologies induced by the metric and the total order, no consensual measure agrees with our visual perception. A measure for the irregularity can help to choose an appropriate ordering scheme for vector-valued mathematical morphology. The following section proposes a measure of irregularity using the Wasserstein metric.

3 Measuring the Irregularity

In this section, we present a measure for the irregularity, referred to as the *global irregularity index*. Although we are interested in measuring the irregularity implied by a total ordering, we will not assume \mathbb{V} is totally ordered. Indeed, the proposed irregularity measure is well defined whenever D is finite and \mathbb{V} is a metric space. For simplicity, however, the value set \mathbb{V}

corresponds to the RGB color space equipped with the Euclidean distance in the following examples and computational experiments.

3.1 The Wasserstein Metric and the Generalized Sum of Pixel-wise Distances

The global irregularity index is given by the relative gap between the Wasserstein metric and a generalized sum of pixel-wise distances. Let us begin by reviewing the generalized sum of pixel-wise distances.

Consider an image operator $\psi : \mathcal{V} \rightarrow \mathcal{V}$. Given an input image $\mathbf{I} \in \mathcal{V}$, let $\mathbf{J} = \psi(\mathbf{I})$ denote the output of the image operator. The generalized sum of pixel-wise distances of \mathbf{I} and \mathbf{J} is an operator $\mathcal{D}_p : \mathcal{V} \times \mathcal{V} \rightarrow [0, +\infty)$ given by

$$\mathcal{D}_p(\mathbf{I}, \mathbf{J}) = \left(\sum_{x \in D} d^p(\mathbf{I}(x), \mathbf{J}(x)) \right)^{\frac{1}{p}}, \quad p \geq 1. \quad (7)$$

The generalized sum of pixel-wise distances is one of the simplest measures that considers the metric d and the pixel locations. However, \mathcal{D}_p is usually not properly scaled, possibly because its dimension is the same as the metric d . For example, the images shown in Figure 1 yield the values $\mathcal{D}_1(\mathbf{I}, \mathbf{J}_L) = 34.12$ and $\mathcal{D}_1(\mathbf{I}, \mathbf{J}_M) = 66.05$. Note that the inequality $\mathcal{D}_1(\mathbf{I}, \mathbf{J}_L) < \mathcal{D}_1(\mathbf{I}, \mathbf{J}_M)$ holds true although \mathbf{J}_L is more irregular than \mathbf{J}_M . Hence, the generalized sum of pixel-wise distances is not an appropriate measure for the irregularity.

Let us now review the Wasserstein metric, also known as the Earth mover's distance or the Kantorovich-Rubinstein distance in some contexts [23, 37]. The Wasserstein metric, named after the Russian mathematician Leonid Vaseršteĭn, has been previously used by Rubner et al. for content-based image retrieval [23]. The Wasserstein metric is formulated as a transport problem and can measure distances between probability distributions [37].

The objective of a transport problem is to minimize the cost to deliver items from n factories to m shops [19]. In our context, the transport problem minimizes the cost to transform the input image \mathbf{I} into the output image \mathbf{J} . The cost is defined using the metric on the value set \mathbb{V} . Precisely, let $V(\mathbf{I}) = \{v_1, \dots, v_n\}$ and $V(\mathbf{J}) = \{u_1, \dots, u_m\}$ be the sets of color values of \mathbf{I} and \mathbf{J} , respectively. Also, let

$$f_i = \text{Card}(\{x : \mathbf{I}(x) = v_i\}) \quad \text{and} \quad g_j = \text{Card}(\{x : \mathbf{J}(x) = u_j\}), \quad (8)$$

denote respectively the number of pixels of value v_i in the image \mathbf{I} and the number of occurrences of the value u_j in \mathbf{J} , for $i = 1, \dots, n$ and $j = 1, \dots, m$. Given $p \geq 1$, the cost to transform a value v_i of \mathbf{I} into a value u_j of \mathbf{J} is defined by

$$c_{ij} = d^p(v_i, u_j), \quad \forall i = 1, \dots, n, \quad \forall j = 1, \dots, m. \quad (9)$$

The Wasserstein metric, denoted by $\mathcal{W}_p : \mathcal{V} \times \mathcal{V} \rightarrow [0, \infty)$ for $p \geq 1$, is given by

$$\mathcal{W}_p(\mathbf{I}, \mathbf{J}) = \left(\sum_{i=1}^n \sum_{j=1}^m c_{ij} x_{ij} \right)^{\frac{1}{p}}, \quad p \geq 1, \quad (10)$$

where x_{ij} solves the linear programming problem

$$\left\{ \begin{array}{l} \text{minimize} \quad \sum_{i=1}^n \sum_{j=1}^m c_{ij} x_{ij} \\ \text{subject to} \quad \sum_{j=1}^m x_{ij} = f_i, \quad \forall i = 1, \dots, n, \\ \quad \quad \quad \sum_{i=1}^n x_{ij} = g_j, \quad \forall j = 1, \dots, m, \\ \quad \quad \quad x_{ij} \geq 0, \quad \forall i = 1, \dots, n, \quad \forall j = 1, \dots, m. \end{array} \right. \quad (11)$$

The Wasserstein metric is the p -th root of the minimal cost to transform \mathbf{I} into \mathbf{J} . In the transport problem (11), the variable x_{ij} represents the (optimal) number of pixels with value v_i of \mathbf{I} transformed to pixels with value u_j of \mathbf{J} . Moreover, the solution of (11), which can be arranged in a matrix $X \in \mathbb{R}^{n \times m}$, is an optimal transport plan. An optimal transport plan is a cyclically monotone plan in the sense that the cost $\sum_{i=1}^n \sum_{j=1}^m c_{ij} x_{ij}$ cannot be improved by changing the number of pixels with value v_i transformed to pixels with value u_j [37]. For the images shown in Figure 1, we obtain $\mathcal{W}_1(\mathbf{I}, \mathbf{J}_L) = 6.18$ and $\mathcal{W}_1(\mathbf{I}, \mathbf{J}_M) = 65.94$. Note that the inequality $\mathcal{W}_1(\mathbf{I}, \mathbf{J}_L) < \mathcal{W}_1(\mathbf{I}, \mathbf{J}_M)$ holds despite \mathbf{J}_L being more irregular than \mathbf{J}_M . Like the generalized sum of pixel-wise distances, the Wasserstein metric is not appropriate for measuring the irregularity.

3.2 The Global Irregularity Index

Although both the generalized sum of pixel-wise distances and the Wasserstein metric are, *per se*, not appropriate to evaluate the irregularity, we advocate that they can be combined to yield a useful measure.

First of all, note that the generalized sum of pixel-wise distances satisfies

$$\mathcal{D}_p(\mathbf{I}, \mathbf{J}) = \left(\sum_{i=1}^n \sum_{j=1}^m c_{ij} y_{ij} \right)^{\frac{1}{p}}, \quad p \geq 1, \quad (12)$$

where

$$y_{ij} = \text{Card}(\{x : \mathbf{I}(x) = v_i \text{ and } \mathbf{J}(x) = u_j, x \in D\}), \quad (13)$$

for all $i = 1, \dots, n$ and $j = 1, \dots, m$. Moreover, it is not hard to see that $y_{ij} \geq 0$ and the identities

$$\sum_{j=1}^m y_{ij} = f_i \quad \text{and} \quad \sum_{i=1}^n y_{ij} = g_j, \quad (14)$$

where f_i and g_j are given by (8), hold for all $i = 1, \dots, n$ and $j = 1, \dots, m$. Therefore, the generalized sum of pixel-wise distances also measures the cost of transforming \mathbf{I} into \mathbf{J} . Because \mathcal{W}_p is the minimal cost, the inequality $\mathcal{W}_p(\mathbf{I}, \mathbf{J}) \leq \mathcal{D}_p(\mathbf{I}, \mathbf{J})$ holds for any \mathbf{I} and $\mathbf{J} = \psi(\mathbf{I})$. The y_{ij} 's given by (13), which can be arranged in a matrix $Y \in \mathbb{R}^{n \times m}$, is called the operator's plan. The operator's plan is probably not an optimal transport plan. Indeed, one usually can reduce the cost $\sum_{i=1}^n \sum_{j=1}^m c_{ij} y_{ij}$ by rerouting the number of pixels with value v_i in \mathbf{I} transformed to pixels with value u_j in \mathbf{J} . In some sense, the difference

$\mathcal{D}_p(\mathbf{I}, \mathbf{J}) - \mathcal{W}_p(\mathbf{I}, \mathbf{J})$ measures the cycles in the operator's plan that can be reduced. Example 1 below illustrates the relationship between cycles and the irregularities introduced by a morphological operator using the toy image shown in Figure 1.

In order to reduce the impact of the metric d on the value set \mathbb{V} and the impact on the choice of the parameter $p \geq 1$, we propose to measure the irregularity using the mapping $\Phi_p^g : \mathcal{V} \times \mathcal{V} \rightarrow [0, 1]$ given by the relative gap between \mathcal{D}_p and \mathcal{W}_p . Precisely, given images $\mathbf{I}, \mathbf{J} \in \mathcal{V}$, we define the global irregularity index by means of the equation

$$\Phi_p^g(\mathbf{I}, \mathbf{J}) = \frac{\mathcal{D}_p(\mathbf{I}, \mathbf{J}) - \mathcal{W}_p(\mathbf{I}, \mathbf{J})}{\mathcal{D}_p(\mathbf{I}, \mathbf{J})}, \quad \text{if } \mathcal{D}_p(\mathbf{I}, \mathbf{J}) \neq 0, \quad (15)$$

and $\Phi_p^g(\mathbf{I}, \mathbf{J}) = 0$ if $\mathcal{D}_p(\mathbf{I}, \mathbf{J}) = 0$. Note that the larger the gap between $\mathcal{W}_p(\mathbf{I}, \mathbf{J})$ and $\mathcal{D}_p(\mathbf{I}, \mathbf{J})$, the larger the global irregularity index. Equivalently, we have

$$\Phi_p^g(\mathbf{I}, \mathbf{J}) = \begin{cases} 0, & \text{if } \mathcal{D}_p(\mathbf{I}, \mathbf{J}) = 0, \\ 1 - \frac{\mathcal{W}_p(\mathbf{I}, \mathbf{J})}{\mathcal{D}_p(\mathbf{I}, \mathbf{J})}, & \text{otherwise.} \end{cases} \quad (16)$$

The irregularity index is symmetric and bounded, that is, $\Phi_p(\mathbf{I}, \mathbf{J}) = \Phi_p(\mathbf{J}, \mathbf{I})$ and $0 \leq \Phi_p(\mathbf{I}, \mathbf{J}) \leq 1$. Moreover, because \mathcal{D}_p and \mathcal{W}_p have the same units and similar magnitudes, $\Phi_p^g(\mathbf{I}, \mathbf{J})$ is a dimensionless quantity. The more irregular is $\mathbf{J} = \psi(\mathbf{I})$, the larger the value of $\Phi_p^g(\mathbf{I}, \mathbf{J})$ is expected to be. For example, the irregularity index of the dilated images \mathbf{J}_L and \mathbf{J}_M shown in Figure 1b) and 1c) are $\Phi_1^g(\mathbf{I}, \mathbf{J}_L) = 81.9\%$ and $\Phi_1^g(\mathbf{I}, \mathbf{J}_M) = 0.17\%$, respectively. The following examples explore further the global irregularity index using toy images.

Example 1 Consider the toy image \mathbf{I} and the dilated image $\mathbf{J}_L = \delta_S^L(\mathbf{I})$ shown in Figure 1. The operator's and the optimal transport plans are arranged respectively in the following matrices:

$$Y = \begin{bmatrix} 156 & 18 & 541 \\ 0 & 1010 & 14 \\ 0 & 0 & 309 \end{bmatrix} \quad \text{and} \quad X = \begin{bmatrix} 156 & 4 & 550 \\ 0 & 1024 & 0 \\ 0 & 0 & 309 \end{bmatrix}. \quad (17)$$

Because $\mathbf{u} = (0, 0, 0)$, $\mathbf{v} = (0, 0, 1)$, and $\mathbf{w} = (1/255, 0, 0)$, we have

$$\mathcal{D}_1(\mathbf{I}, \mathbf{J}_L) = 18d(\mathbf{u}, \mathbf{v}) + 541d(\mathbf{u}, \mathbf{w}) + 14d(\mathbf{v}, \mathbf{w}) = 34.12, \quad (18)$$

$$\mathcal{W}_1(\mathbf{I}, \mathbf{J}_L) = 4d(\mathbf{u}, \mathbf{v}) + 555d(\mathbf{u}, \mathbf{w}) = 6.18, \quad (19)$$

and

$$\mathcal{D}_1(\mathbf{I}, \mathbf{J}_L) - \mathcal{W}_1(\mathbf{I}, \mathbf{J}_L) = 14(d(\mathbf{u}, \mathbf{v}) + d(\mathbf{v}, \mathbf{w}) - d(\mathbf{u}, \mathbf{w})) = 27.95, \quad (20)$$

From (20), we conclude that the cost of the operator's plan can be reduced by replacing 14 times the route $\mathbf{u} \rightarrow \mathbf{v} \rightarrow \mathbf{w}$ by $\mathbf{u} \rightarrow \mathbf{w}$ or, equivalently, by avoiding the cycle (\mathbf{u}, \mathbf{v}) , (\mathbf{v}, \mathbf{w}) , (\mathbf{w}, \mathbf{u}) . Moreover, note that the route $\mathbf{u} \rightarrow \mathbf{v} \rightarrow \mathbf{w}$ reflects the lexicographical inequalities $\mathbf{u} \leq_L \mathbf{v} \leq_L \mathbf{w}$. Thus, the difference $\mathcal{D}_1(\mathbf{I}, \mathbf{J}_L) - \mathcal{W}_1(\mathbf{I}, \mathbf{J}_L)$ is proportional to the number of pixels with irregular values (14 in this example) as well as to the distance between the pixel values (in this example, the amount $d(\mathbf{u}, \mathbf{v}) + d(\mathbf{v}, \mathbf{w}) - d(\mathbf{u}, \mathbf{w})$). The global irregularity index is obtained by dividing the difference $\mathcal{D}_1(\mathbf{I}, \mathbf{J}_L) - \mathcal{W}_1(\mathbf{I}, \mathbf{J}_L)$ by $\mathcal{D}_1(\mathbf{I}, \mathbf{J}_L)$, that is,

$$\Phi_1^g(\mathbf{I}, \mathbf{J}_L) = \frac{\mathcal{D}_1(\mathbf{I}, \mathbf{J}_L) - \mathcal{W}_1(\mathbf{I}, \mathbf{J}_L)}{\mathcal{D}_1(\mathbf{I}, \mathbf{J}_L)} = \frac{27.95}{34.12} = 0.819. \quad (21)$$

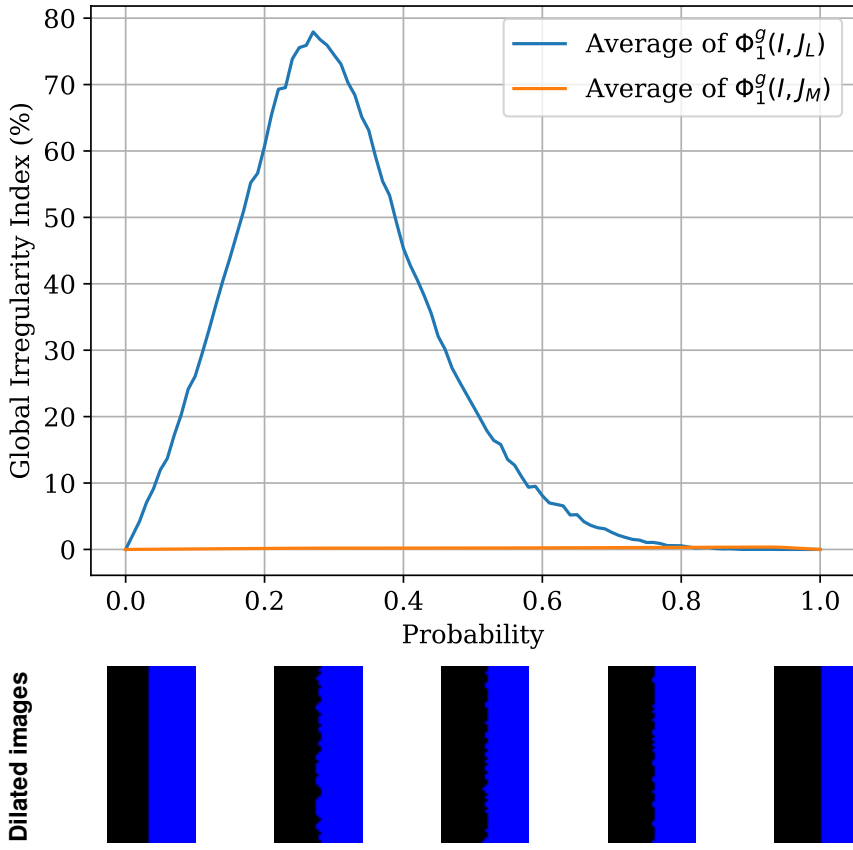


Fig. 2 Top: Global irregularity index by the probability of replacing a pure black pixel value $u = (0, 0, 0)$ by the black $w = (0.005, 0, 0)$ in an image similar to Figure 1a). **Bottom:** Lexicographical dilation of images obtained using $\pi = 0.0, 0.25, 0.5, 0.75$, and 1.0 , respectively.

Example 2 Figure 2 shows the percentage of the global irregularity index computed on dilated versions of toy images similar to the one provided by Chevallier and Angulo [6]. Precisely, we first construct an image of size 64×32 with two stripes of the same width but with the pure colors black $u = (0, 0, 0)$ and blue $v = (0, 0, 1)$. Then, a pure black pixel value is replaced by the black $w = (1/255, 0, 0)$ with probability $\pi \in [0, 1]$. The resulting image I is dilated by a cross structuring element using both the lexicographical and the marginal ordering schemes, yielding the images J_L and J_M , respectively. The simulation has been repeated 500 times for each probability $\pi \in [0, 1]$. Figure 2 shows the average of the global irregularity index by the probability π . For a better interpretation of this plot, dilated samples of the images generated with probabilities $\pi = 0.0, 0.25, 0.50, 0.75$, and 1 are shown at the bottom of Figure 2. Note that the irregularity index for the lexicographical RGB ordering increases until close to $\pi = 0.3$ and then decreases. Furthermore, the irregularity indexes agree with the visual irregularity provided in the sample images at the bottom of Figure 2. In contrast, the marginal approach yields small irregularity indexes. This toy example confirms our expectation that the more irregular is the image $J = \psi(I)$, the larger is the global irregularity index $\Phi_1^g(I, J)$.

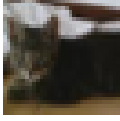
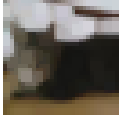
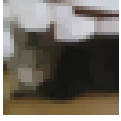

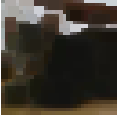



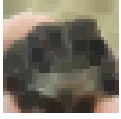















	Original img.	Marginal	Loewner	Lex. RGB	SVM-based	Proj. Depth
Dilation						
		0.93%	0.87%	1.37%	8.60%	5.38%
Erosion						
		0.93%	0.86%	1.36%	12.04%	45.27%
Opening						
		2.79%	2.83%	7.07%	34.84%	31.13%
Closing						
		2.61%	2.68%	6.33%	21.26%	74.53%

Fig. 3 Illustrative examples of the global irregularity index Φ_1^g computed for several tiny color images using different morphological operators.

3.3 Computational Experiments with Tiny Color Images

Let us now provide some computational experiments with tiny color images². Precisely, we compute the global irregularity index Φ_1^g of morphological operators applied on one hundred color images from the CIFAR10 dataset. The measures have been computed using erosion, dilation, opening, and closing by a 3×3 square structuring element. Specifically, we have computed twenty-five dilations, erosions, openings, and closings on different images from the CIFAR10 dataset.

We considered three approaches based on total orderings. The first is the RGB lexicographical order in which the colors are ranked sequentially according to the red, green, and blue channels. The other two approaches are based on reduced orderings [36]. Specifically, we considered the supervised reduced ordering based on an SVM with radial basis function kernel [34]. In this computational experiment, we trained the SVM to distinguish the central object on an image from the rest. The last approach uses an unsupervised reduced ordering based on the random projection depth, which aims to discriminate between background and foreground pixels [35]. For comparison, we also include two approaches based on partial orderings. Namely, the marginal approach and the approach based on Loewner order [5]. Because these two approaches are not based on total orders, their output images are not expected to be very irregular.

Figure 3 depicts some original images, the outcome of a morphological operator, and the corresponding global irregularity index. The images in the first column correspond to the original color images. The following columns present the output of morphological op-

² The Julia's source-code for the global irregularity index is available at <https://github.com/mevalle/Irregularity-Index>.

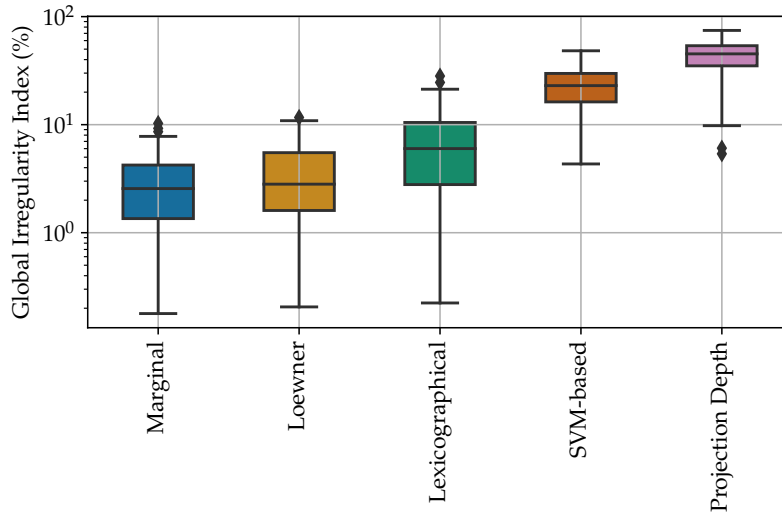


Fig. 4 The boxplot of the global irregularity index of dilations, erosions, openings, and closings for 100 color images of size 32×32 using five different morphological approaches.

erators defined using the marginal, Loewner, lexicographical RGB, supervised SVM-based, and projection depth approaches, respectively. We provide the global irregularity index below the images produced by the morphological operators. As expected, the marginal and the Loewner approaches yielded global irregularity indexes smaller than the lexicographical, SVM-based, and projection depth approaches. The supervised SVM-based approach yielded the most irregular dilated image. The irregularity index of 5.38% produced by projection depth's dilation of the cat image is an outlier of the global irregularity index produced by this unsupervised morphological approach. Indeed, the median of the global irregularity index produced by the morphological operators based on the projection depth is 45.22%. The eroded image depicted in the last column of Figure 3 is a typical outcome of the projection depth approach. The median of the irregularity indexes produced by the marginal, Loewner, lexicographical, and the SVM-based approaches are 2.56%, 2.81%, 6%, and 22.98%, respectively. The truck image's openings and the car image's closings provide typical examples of the global irregularity index produced by the marginal, Loewner, and lexicographical approaches. The opening of the car image produced by the projection depth approach yielded the largest global irregularity index of this experiment.

The boxplot shown in Figure 4 summarizes the outcome of this computational experiment. As expected, the morphological operators based on the marginal and the Loewner partial orderings resulted in minor global irregularity indexes. In contrast, the morphological operators based on the lexicographical RGB, SVM-based, and the projection depth yielded the largest global irregularity indexes. Accordingly, the morphological approaches can be ranked increasingly using the global irregularity index as follows: marginal, Loewner, lexicographical RGB, supervised SVM-based, and projection depth. We confirmed the ranking of the morphological approaches statistically using the Wilcoxon signed-rank test with a confidence level of 99%. Concluding, the morphological operators based on total orderings yielded more significant global irregularity indexes than the morphological operators obtained using partial orderings.

Finally, we would like to emphasize that neither the generalized sum of pixel-wise distances nor the Wasserstein metric are appropriate for measuring the irregularity of morphological operators. For example, the generalized sum of pixel-wise distances and the Wasserstein metric between the original and the eroded frog image produced by the marginal approach are 182.31 and 180.61, respectively. Similarly, the same measures between the original and the eroded frog image produced by the projection depth approach are 135.44 and 74.13. Although the projection depth approach yielded a smaller generalized sum of pixel-wise distances and Wasserstein metric values, the former outcome is a visually more irregular image than the image produced by the marginal approach. Conversely, a more irregular image does not necessarily result in a smaller generalized sum of pixel-wise distances or a smaller Wasserstein metric value. Indeed, the generalized sum of pixel-wise distances and the Wasserstein metric between the original truck and its opening by the marginal approach are 31.05 and 30.18, respectively. The same measures applied to the original truck and its closing by the projection depth approach are 53.96 and 37.17. However, the projection depth approach visually yielded a more irregular truck image than the opening by the marginal approach.

4 Computing the Irregularity Index

Despite its mathematical formulation, computing the global irregularity index is not an easy task for natural images. Precisely, the irregularity index requires solving a linear programming problem with mn variables, where m and n are the numbers of distinct pixel values of the images \mathbf{I} and \mathbf{J} , respectively. As a consequence, the complexity for computing the global irregularity index analytically grows as $\mathcal{O}(m^3 n^3 \log(mn))$ [20]. In practical situations, the dimension of the linear programming problem (11) is enormous, making it impossible to compute the global irregularity index analytically in real-time. We propose to compute the Wasserstein metric and the generalized sum of pixel-wise distances locally and aggregate the values into a single index to circumvent this computational burden.

4.1 The Local Irregularity Index

Let $\{W_1, W_2, \dots, W_k\}$ be a partition of the image domain D , that is, W_1, W_2, \dots, W_k are non-overlapping local windows such that $D = \cup_{i=1}^k W_i$. Also, let $\mathcal{W}_p(\mathbf{I}, \mathbf{J}|W_\ell)$ denote the Wasserstein metric computed restricting the images \mathbf{I} and \mathbf{J} to the local window W_ℓ . The local irregularity index is defined by the following equation for all $\mathbf{I}, \mathbf{J} \in \mathcal{V}$:

$$\Phi_p^l(\mathbf{I}, \mathbf{J}) = 1 - \frac{\left(\sum_{\ell=1}^k (\mathcal{W}_p(\mathbf{I}, \mathbf{J}|W_\ell))^p \right)^{1/p}}{\mathcal{D}_p(\mathbf{I}, \mathbf{J})}. \quad (22)$$

The size of the local windows W_1, \dots, W_k plays an important role in the local irregularity index. On the one hand, it is impractical to compute the irregularity index using large local windows. On the other hand, the local irregularity index approaches zero as the size of the local windows decreases. Thus, the size of the local windows is a trade-off between computational cost and accuracy of the local irregularity index.

Remark 1 We would like to point out that we previously used the geometric mean to aggregate the quotient of $\mathcal{W}_p(\mathbf{I}, \mathbf{J}|W_\ell)$ by $\mathcal{D}_p(\mathbf{I}, \mathbf{J}|W_\ell)$ [30]. However, the geometric mean does not scale well for moderate and large size images because $0 < \frac{\mathcal{W}_p(\mathbf{I}, \mathbf{J}|W_\ell)}{\mathcal{D}_p(\mathbf{I}, \mathbf{J}|W_\ell)} < 1$ implies $\prod_{\ell=1}^k \frac{\mathcal{W}_p(\mathbf{I}, \mathbf{J}|W_\ell)}{\mathcal{D}_p(\mathbf{I}, \mathbf{J}|W_\ell)} \rightarrow 0$ as the number k of local windows increases. In this paper, the local irregularity index is given by (22) which, besides scaling well to moderate and large scale images, is closely related to the minibatch Wasserstein metric [8].

The local irregularity index provides a lower bound to the global irregularity index, i.e., the inequality $\Phi_p^l(\mathbf{I}, \mathbf{J}) \leq \Phi_p^g(\mathbf{I}, \mathbf{J})$ holds true for all $\mathbf{I} \in \mathcal{V}$ and $\mathbf{J} = \psi(\mathbf{I})$. Precisely, let

$$f_i^\ell = \text{Card}(\{x \in W_\ell : \mathbf{I}(x) = v_i\}) \quad \text{and} \quad g_j^\ell = \text{Card}(\{x \in W_\ell : \mathbf{J}(x) = u_j\}), \quad (23)$$

denote respectively the number of pixels of \mathbf{I} with value v_i and the number of pixels of \mathbf{J} with value u_j , both restricted to the local window W_ℓ , for $\ell = 1, \dots, k$, $i = 1, \dots, n$, and $j = 1, \dots, m$. Note that $f_i^\ell = 0$ and $g_j^\ell = 0$ if the images \mathbf{I} and \mathbf{J} have no pixels with values v_i and u_j in the windows W_ℓ , respectively. Moreover, since $\{W_\ell : \ell = 1, \dots, k\}$ is a partition of the images domain D , the identities

$$\sum_{\ell=1}^k f_i^\ell = f_i \quad \text{and} \quad \sum_{\ell=1}^k g_j^\ell = g_j, \quad (24)$$

where f_i and g_j are given by (8), hold for all $i = 1, \dots, n$ and $j = 1, \dots, m$. Although in practice we compute $\mathcal{W}_p(\mathbf{I}, \mathbf{J}|W_\ell)$ using only the pixel values of \mathbf{I} and \mathbf{J} in the local window W_ℓ , the restricted Wasserstein metric satisfies

$$(\mathcal{W}_p(\mathbf{I}, \mathbf{J}|W_\ell))^p = \sum_{i=1}^n \sum_{j=1}^m c_{ij} x_{ij}^\ell, \quad (25)$$

where x_{ij}^ℓ solves the linear programming problem

$$\begin{cases} \text{minimize} & \sum_{i=1}^n \sum_{j=1}^m c_{ij} x_{ij}^\ell \\ \text{subject to} & \sum_{j=1}^m x_{ij}^\ell = f_i^\ell, \quad \sum_{i=1}^n x_{ij}^\ell = g_j^\ell, \quad \text{and} \quad x_{ij}^\ell \geq 0, \quad \forall i, \forall j. \end{cases} \quad (26)$$

Now, define the non-negative variables

$$z_{ij} = \sum_{\ell=1}^k x_{ij}^\ell, \quad \forall i = 1, \dots, n \text{ and } \forall j = 1, \dots, m. \quad (27)$$

From (24), we conclude that

$$\sum_{j=1}^m z_{ij} = \sum_{j=1}^m \sum_{\ell=1}^k x_{ij}^\ell = \sum_{\ell=1}^k f_i^\ell = f_i \quad \text{and} \quad \sum_{i=1}^n z_{ij} = \sum_{\ell=1}^k g_j^\ell = g_j. \quad (28)$$

Thus, the variables z_{ij} satisfy the constraints of the linear programming problem (11). Because $(\mathcal{W}_p(\mathbf{I}, \mathbf{J}))^p$ is the minimum value of (11), from (25) we conclude that

$$(\mathcal{W}_p(\mathbf{I}, \mathbf{J}))^p \leq \sum_{i=1}^n \sum_{j=1}^m c_{ij} z_{ij} = \sum_{\ell=1}^k \sum_{i=1}^n \sum_{j=1}^m c_{ij} x_{ij}^\ell = \sum_{\ell=1}^k (\mathcal{W}_p(\mathbf{I}, \mathbf{J}|W_\ell))^p, \quad (29)$$

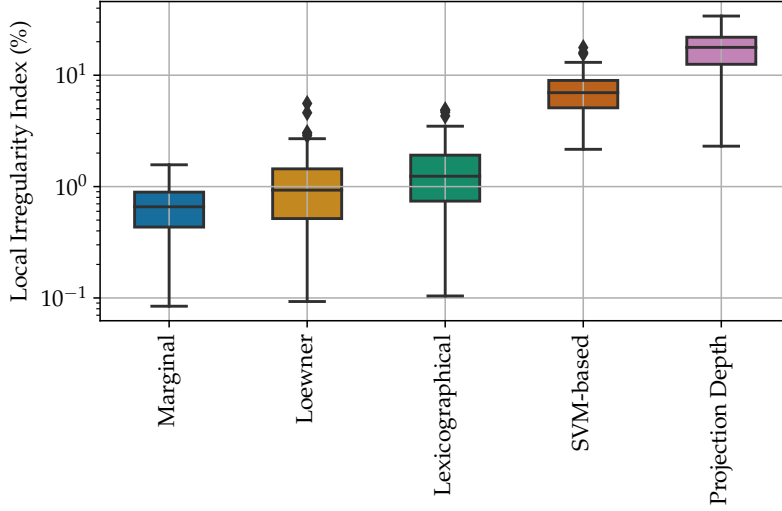


Fig. 5 The boxplot of the local irregularity index with local windows of size 16×16 obtained from dilations, erosions, openings, and closings for 100 natural color images using five different morphological approaches.

which results in the desired inequality

$$\Phi_p^g(\mathbf{I}, \mathbf{J}) = 1 - \frac{(\mathcal{W}_p(\mathbf{I}, \mathbf{J}))^p}{\mathcal{D}_p(\mathbf{I}, \mathbf{J})} \geq 1 - \frac{\left(\sum_{\ell=1}^k (\mathcal{W}_p(\mathbf{I}, \mathbf{J}|W_\ell))^p\right)^{\frac{1}{p}}}{\mathcal{D}_p(\mathbf{I}, \mathbf{J})} = \Phi_p^l(\mathbf{I}, \mathbf{J}), \quad (30)$$

for all $\mathbf{I} \in \mathcal{V}$ and $\mathbf{J} = \psi(\mathbf{I})$.

4.2 Computational Experiments with Natural Color Images

In analogy to the previous section, let us perform some computational experiments with natural color images. However, instead of computing the global irregularity index on tiny color images from the CIFAR10 dataset, we compute the local irregularity index Φ_1^l of morphological operators applied on one hundred colors images from the Berkeley segmentation dataset³. The local irregularity index is computed using local windows of size 16×16 for dilations, erosions, openings, and closings by a 9×9 square structuring element. The boxplot shown in Figure 5 summarizes the outcome of this computational experiment.

Note from Figure 5 that the approaches based on partial orderings, namely the marginal and the Loewner approaches, yielded the minor local irregularity indexes. In contrast, the approaches based on total orderings produced the largest irregularity indexes. Using the Wilcoxon signed-rank test with a confidence level at 99%, we rank the local irregularity indexes increasingly by the marginal, Loewner, lexicographical RGB, supervised SVM-based, and the projection depth approaches.

Figures 6–9 provide illustrative examples of images produced by the morphological operators together with the corresponding local irregularity index. As expected, the marginal

³ The Julia's source-code for the local irregularity index is available at <https://github.com/mevalle/Irregularity-Index>.



Fig. 6 Original color image and the corresponding dilation by a 9×9 square produced by the marginal, the Loewner, lexicographical, SVM-based, and projection depth approaches. The local irregularity index, obtained using local windows of size 16×16 , is given together with the dilated images.

and the Loewner approaches produced the smallest local irregularity indexes among the dilated images shown in Figure 6. In contrast, the SVM-based and the projection depth approaches yielded the largest local irregularity indexes. We would like to point out that the value of 2.31% is an outlier corresponding to the smallest local irregularity index produced by the projection depth approach on the one hundred natural color images considered in this computational experiment. Similarly, Figure 7 depicts an original color image and the corresponding eroded images. The SVM-based and the projection depth approaches again yielded the most significant local irregularity indexes. Furthermore, in contrast to the outlier irregularity value attained by the dilated image shown in Figure 6, the eroded image in Figure 7 is a typical image produced by the projection depth approach in this experiment. Other typical images produced by the five morphological approaches are shown in Figures 8 and 9.

We would like to conclude this subsection by calling the reader's attention to the qualitative similarity between the boxplots shown in Figures 4 and 5. Apart from a scaling factor,



Fig. 7 Original color image and the corresponding erosion by a 9×9 square produced by the marginal, the Loewner, lexicographical, SVM-based, and projection depth approaches. The local irregularity index, obtained using local windows of size 16×16 , is given together with the eroded images.

the global and local irregularity represents well the visual irregularity introduced by the morphological operators. Moreover, although the local irregularity index yields a lower bound for the global irregularity index, we advocate its use for measuring the irregularity of vector-valued morphological operators.

4.3 Entropic regularized methods for approximating the Wasserstein metric

Besides partitioning the domain of a vector-valued image into local windows, we can further reduce the computational cost for computing the irregularity index by considering entropic regularized methods for approximating the analytical Wasserstein metric. In a few words, entropic regularized methods like the Sinkhorn method and its stabilized version add an entropic penalty to the original transport problem. In mathematical terms, the entropic reg-

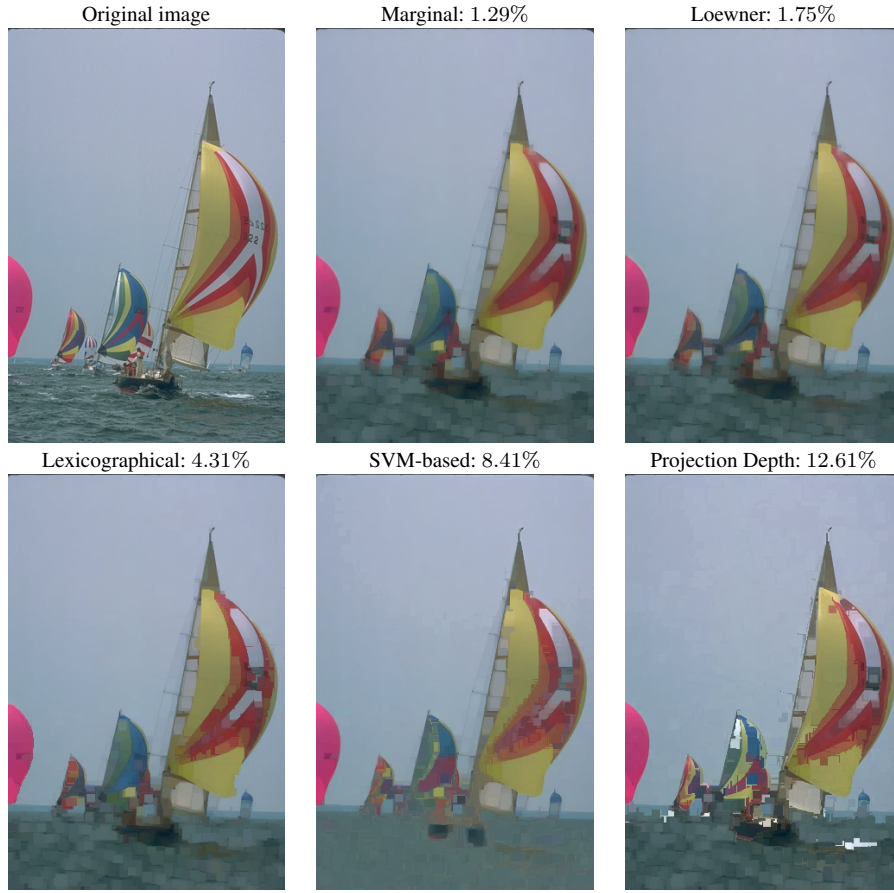


Fig. 8 Original color image and the corresponding opening by a 9×9 square produced by the marginal, the Loewner, lexicographical, SVM-based, and projection depth approaches. The local irregularity index, obtained using local windows of size 16×16 , is given together with the opening images.

ularized methods aim to solve the convex optimization problem

$$\left\{ \begin{array}{l} \text{minimize} \quad \sum_{i=1}^n \sum_{j=1}^m c_{ij} x_{ij} + \epsilon \sum_{i=1}^n \sum_{j=1}^m x_{ij} (\log(x_{ij}) - 1) \\ \text{subject to} \quad \sum_{j=1}^m x_{ij} = f_i / N_D, \quad \forall i = 1, \dots, n, \\ \sum_{i=1}^n x_{ij} = g_j / N_D, \quad \forall j = 1, \dots, m, \\ x_{ij} \geq 0, \quad \forall i = 1, \dots, n, \forall j = 1, \dots, m. \end{array} \right. \quad (31)$$

where $\epsilon > 0$ is a regularization term and N_D denotes the number of pixels of the processed images. Note that, for obtaining a meaningful entropic regularization, the variables x_{ij} must satisfy $\sum_{i=1}^n \sum_{j=1}^m x_{ij} = (1/N_D) \sum_{i=1}^n f_i = (1/N_D) \sum_{j=1}^m g_j = 1$. The Wasserstein



Fig. 9 Original color image and the corresponding opening by a 9×9 square produced by the marginal, the Loewner, lexicographical, SVM-based, and projection depth approaches. The local irregularity index, obtained using local windows of size 16×16 , is given together with the opening images.

metric is then approximated by

$$\mathcal{W}_p^r(\mathbf{I}, \mathbf{J}) = \left(N_D \sum_{i=1}^n \sum_{j=1}^m c_{ij} x_{ij} \right)^{1/p}, \quad p \geq 1, \quad (32)$$

where x_{ij} solves (31). Note that the approximation \mathcal{W}_p^r is computed without the regularization term. Since both (11) and (31) have equivalent constraints (they differ only because of the term N_D), the inequality $\mathcal{W}_p(\mathbf{I}, \mathbf{J}) \leq \mathcal{W}_p^r(\mathbf{I}, \mathbf{J})$ holds for all image \mathbf{I} and $\mathbf{J} = \psi(\mathbf{I})$. As a consequence, the irregularity index computed by an entropic regularized method also yields a lower bound for the analytical irregularity index.

As pointed out by Peyré and Cuturi [19], the objective in (31) is an ϵ -strongly convex function. Therefore, the regularized optimization problem has a unique optimal solution. Furthermore, the optimal solution can be computed using the Sinkhorn method, which uses only matrix-vector products and, thus, it is suited to be executed in GPU. Also, the unique

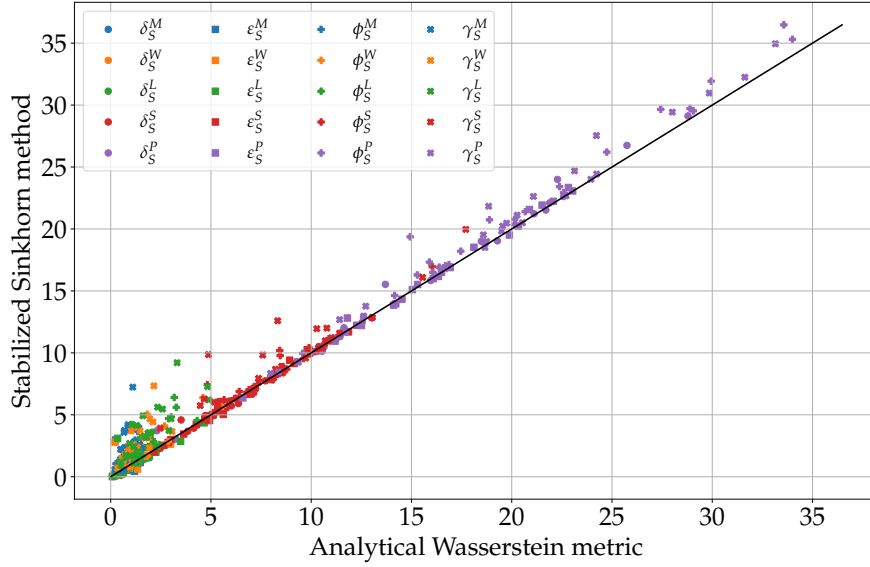


Fig. 10 Scatter plot of the local irregularity index computed using the analytical Wasserstein metric and the stabilized Sinkhorn method with regularization term $\epsilon = 10^{-3}$, both with local windows of size 16×16 .

solution of (31) converges to the analytical solution as ϵ tends to zero. On the downside, the convergence of the Sinkhorn method slows as the entropic term approaches zeros. For small ϵ , the regularized optimization problem defined by (31) can be solved using stabilized versions of the Sinkhorn method [26]. The Sinkhorn method and its stabilized versions are implemented in optimal transport libraries such as the Python Optimal Transport⁴ (POT) and Julia's Optimal Transport⁵.

Figure 10 compares the local irregularity index computed using an entropic regularized optimal transport method with the analytical Wasserstein metric. Precisely, the scatter plot in Figure 10 shows the local irregularity index computed on the considered subset of the Berkeley segmentation dataset. Similarly to the previous experiments, we considered dilations (δ_S), erosions (ϵ_S), openings (γ_S), and closings (ϕ_S) by a 9×9 square structuring element S . We distinguished the marginal, Loewner, lexicographical, SVM-based, and projection depth approaches using the superindexes M , W , L , S , and P , respectively. The horizontal and the vertical axes in the scatter plot shown in Figure 10 correspond to the local irregularity index obtained using the analytical and the stabilized Sinkhorn method, respectively. In this computational experiment, we have used the regularization term $\epsilon = 10^{-3}$. Figure 10 also shows the line $y = x$. The closer a point is to the line $y = x$, the better is the approximation obtained by the stabilized Sinkhorn method to the analytical solution. Notably, the coefficient of determination obtained from the 500 points is $R^2 = 0.98$. Thus, the stabilized Sinkhorn method yielded good estimations for the analytical local irregularity index using local windows of size 16×16 . Furthermore, computing the local irregularity index by the stabilized Sinkhorn method is much faster than using the analytical Wasser-

⁴ <https://optimaltransport.github.io/>

⁵ <https://github.com/JuliaOptimalTransport/OptimalTransport.jl>

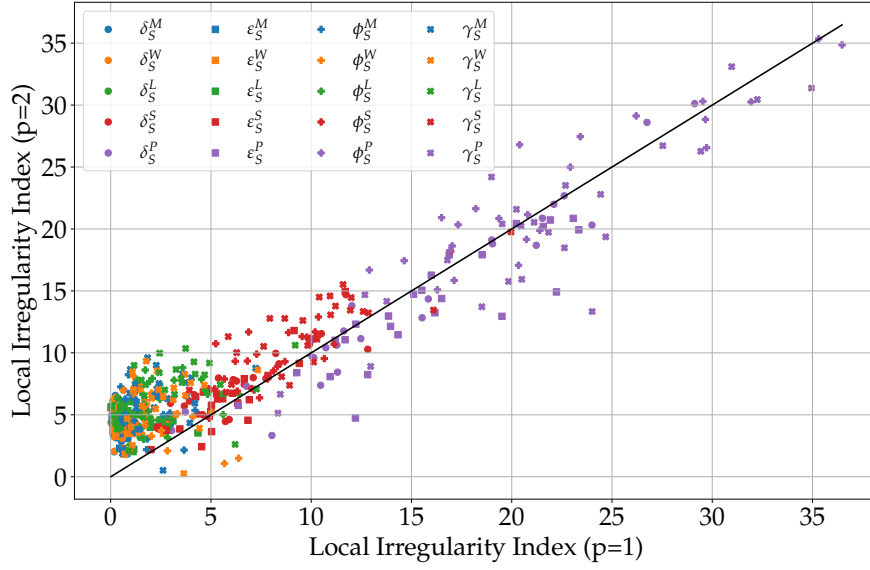


Fig. 11 Scatter plot of the local irregularity index computed using the parameters $p = 1$ and $p = 2$.

stein metric. Thus, we encourage computing the local irregularity index using the Sinkhorn method or its variations. We would like to point out that other methods, such as sliced approximations of the optimal transport problem [20, 21], can also be considered for estimating the irregularity index.

4.4 Additional Remarks on the Local Irregularity Index

Let us finish this section by briefly addressing the sensibility of the local irregularity index with respect to the parameter p . Let us also address the role of the sizes of the local windows and the structuring element on the local irregularity index.

First, analogous to Figure 10, Figure 11 compares the local irregularity index obtained using $p = 1$ and $p = 2$. In Figure 11, a point above the line $y = x$ means that the local irregularity index for $p = 1$ is smaller than for $p = 2$, that is, $\Phi_1^l(\mathbf{I}, \mathbf{J}) < \Phi_2^l(\mathbf{I}, \mathbf{J})$. Conversely, the inequality $\Phi_1^l(\mathbf{I}, \mathbf{J}) > \Phi_2^l(\mathbf{I}, \mathbf{J})$ yields a point below the line $y = x$. Although the local irregularity index is predominantly larger for $p = 2$ than for $p = 1$, they are similar for values greater than 5%. Indeed, the coefficient of determination increases from 0.77 for the 500 images to 0.89 restricting both $\Phi_1^l(\mathbf{I}, \mathbf{J}) > 5\%$ and $\Phi_2^l(\mathbf{I}, \mathbf{J}) > 5\%$. The less irregular the morphological operator is, the more significant is the parameter p to the irregularity index. Indeed, although the local irregularity index with $p = 2$ ranked the approaches based on the total orders well, it could not distinguish the irregularity introduced by the morphological operators based on the marginal and the Loewner orders.

Let us now turn our attention to the size of the local windows and the structuring element. We consider square structuring elements of size $3 \times 3, 5 \times 5, \dots, 25 \times 25$ and local windows of size $4 \times 4, 8 \times 8, 16 \times 16$, and 32×32 . Figure 12 shows the median of the local irregularity index by the size of the structuring element obtained by considering four

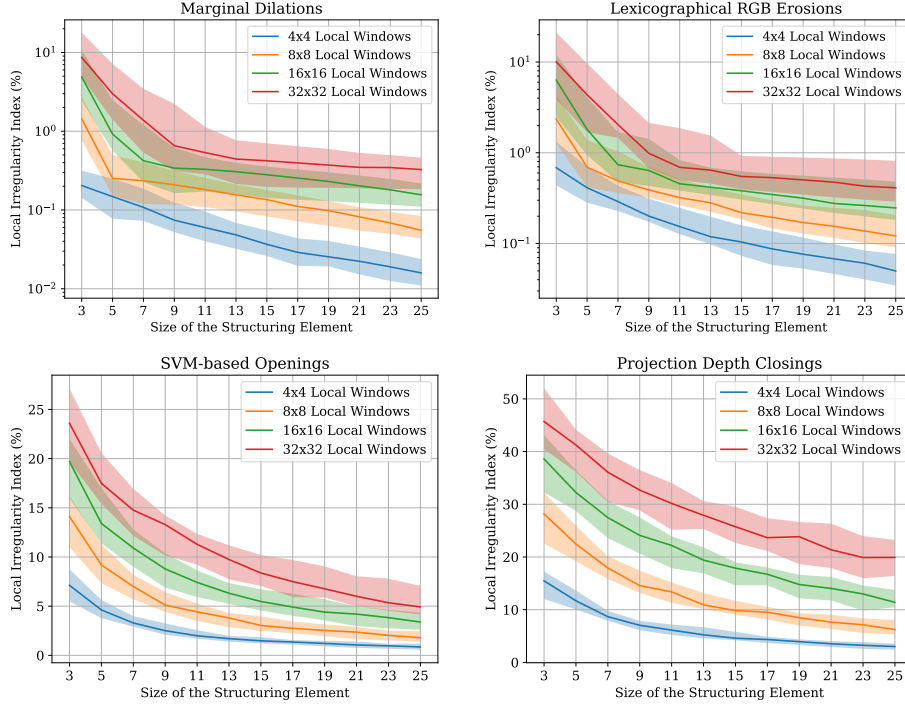


Fig. 12 Local irregularity index by the size of the structuring element. The first and third quartiles delimit the filled area.

different local windows. The area between the first and third quartiles is also included in Figure 12. Note from Figure 12 that the local irregularity index decreases with the size of the structuring element independently of the local windows. Moreover, there is no clear relationship between the size of the local windows and the structuring element. In particular, the local window does not need to be larger nor smaller than the structuring element.

Also, note that the local irregularity index increases with the size of the local windows. Despite the noticeable differences between the median of the local irregularity index, the filled area between the first and third quartiles overlaps for local windows of size 16×16 and 32×32 for some approaches. Accordingly, the local irregularity index should converge to the global irregularity index as the size of the local windows increases. Finally, although we face a trade-off between computational cost and approximating the global irregularity index, fixed local windows can be confidently used for comparing the irregularity of different morphological operators or approaches.

5 Concluding Remarks

Despite the rigorous formulation of the irregularity issue provided by Chevallier and Angulo [6], as far as we know, there was no effective measure for this problem. This paper proposed two measures for the irregularity of morphological operators: the global and the local irregularity indexes, denoted by Φ_p^g and Φ_p^l respectively. The global irregularity index is given by the relative gap between the Wasserstein metric \mathcal{W}_p and the generalized sum of pixel-wise

distances \mathcal{D}_p . The computational experiments detailed in Section 3 confirmed good values for the irregularity of tiny color images. However, in practical situations, the number of distinct pixel values makes it impossible to compute the global irregularity index. We proposed computing the irregularity index on several non-overlapping local windows to circumvent this computational drawback, resulting in the local irregularity index. Furthermore, the computational cost can be reduced significantly by replacing the analytical Wasserstein metric with entropic regularized approximations of the optimal transport problem, such as the one produced by the Sinkhorn or the stabilized Sinkhorn methods [19, 26]. The computational experiments detailed in Section 3 confirmed the practical application of the local irregularity index as a measure of the irregularity in natural color images. Indeed, besides the illustrative examples provided in Figures 6-9, we provided a statistical analysis with one hundred natural images from the Berkeley segmentation dataset using four different morphological operators obtained from five vector-valued approaches.

Finally, we would like to point out that the irregularity index can be used in the future to evaluate the performance of morphological operators. The irregularity index can also be used for the design of efficient morphological operators. For example, it can be used as the objective function for the design of vector-valued morphological operators based on uncertain reduced orderings [25].

Appendix A Supervised and Unsupervised Morphological Approaches

Let us briefly review the supervised and unsupervised vector-valued morphological approaches, whose details can be found in [34, 35].

In a supervised ordering, the surjective mapping $\rho : \mathbb{V} \rightarrow \mathbb{L}$ is defined using a set $F \subset \mathbb{V}$ of foreground values and a set $B \subset \mathbb{V}$ of background values such that $F \cap B = \emptyset$. Given the sets F and B , the mapping ρ is expected to satisfy the inequality $\rho(\mathbf{f}) > \rho(\mathbf{b})$ for $\mathbf{f} \in F$ and $\mathbf{b} \in B$. Considering $\mathbb{V} \subset \mathbb{R}^d$ and $\mathbb{L} \subset \mathbb{R}$, the decision function of a SVM can be used to accomplish this goal [27, 32, 34]. Precisely, consider sets $F = \{\mathbf{f}_1, \dots, \mathbf{f}_K\} \subset \mathbb{R}^d$ and $B = \{\mathbf{b}_1, \dots, \mathbf{b}_M\} \subset \mathbb{R}^d$ of foreground and background values, respectively. An SVM-based morphological approach is obtained by considering the mapping $\rho_S : \mathbb{R}^d \rightarrow \mathbb{R}$ given by

$$\rho_S(\mathbf{x}) = \sum_{\mathbf{f} \in F} \alpha_i \kappa(\mathbf{x}, \mathbf{f}) - \sum_{\mathbf{b} \in B} \beta_j \kappa(\mathbf{x}, \mathbf{b}), \quad \forall \mathbf{x} \in \mathbb{R}^d, \quad (33)$$

where $\kappa : \mathbb{R}^d \times \mathbb{R}^d \rightarrow \mathbb{R}$ is a Mercer kernel [27]. For example, Gaussian radial basis function kernel is given by

$$\kappa(\mathbf{x}, \mathbf{y}) = e^{-\frac{1}{2\sigma} \|\mathbf{x} - \mathbf{y}\|_2^2}, \quad \forall \mathbf{x}, \mathbf{y} \in \mathbb{R}^d, \quad (34)$$

where $\sigma > 0$ is a parameter. Moreover, $\alpha_1, \dots, \alpha_K$ and β_1, \dots, β_M solve the quadratic optimization problem

$$\left\{ \begin{array}{l} \text{maximize} \quad \sum_{i=1}^K \alpha_i + \sum_{j=1}^M \beta_j - \frac{1}{2} \sum_{i,l=1}^K \alpha_i \alpha_l \kappa(\mathbf{f}_i, \mathbf{f}_l) - \frac{1}{2} \sum_{j,l=1}^M \beta_j \beta_l \kappa(\mathbf{b}_j, \mathbf{b}_l) \\ \quad + \frac{1}{2} \sum_{i=1}^K \sum_{j=1}^M \alpha_i \beta_j \kappa(\mathbf{f}_i, \mathbf{b}_j) \\ \text{subject to} \quad \sum_{i=1}^K \alpha_i - \sum_{j=1}^M \beta_j = 0, \\ \quad 0 \leq \alpha_i, \beta_j \leq C, \end{array} \right. \quad (35)$$

where the parameter $C > 0$ controls the trade-off between the classification error and the margin of separation between background and foreground values [13, 27].

In an unsupervised morphological approach, the mapping $\rho : \mathbb{V} \rightarrow \mathbb{L}$ is determined using a set of unlabeled values. The statistical depth projection-based approach, for example, determines the mapping ρ based on “anomalies” with respect to a background composed of the majority of pixel values of an image [35]. Formally, suppose $\mathbb{V} \subset \mathbb{R}^d$ and $\mathbb{L} \subset \mathbb{R}$. Given a training sample represented by a matrix $\mathbf{X} = [\mathbf{x}_1, \dots, \mathbf{x}_n] \in \mathbb{R}^{d \times n}$, the projection depth function $\rho_P^* : \mathbb{R}^d \rightarrow \mathbb{R}$ is defined by

$$\rho_P^*(\mathbf{x}) = \sup_{\mathbf{u} \in \mathbb{S}^{d-1}} \frac{|\mathbf{u}^T \mathbf{x} - \text{MED}(\mathbf{u}^T \mathbf{X})|}{\text{MAD}(\mathbf{u}^T \mathbf{X})}, \quad \forall \mathbf{x} \in \mathbb{R}^d, \quad (36)$$

where $\mathbb{S}^{d-1} = \{\mathbf{x} \in \mathbb{R}^d : \|\mathbf{x}\|_2 = 1\}$, $\text{MED} : \mathbb{R}^n \rightarrow \mathbb{R}$ is the median operator, and $\text{MAD} : \mathbb{R}^n \rightarrow \mathbb{R}$ is the median absolute deviation from the median operator. Recall that the median absolute deviation from the median is given by

$$\text{MAD}(\mathbf{t}) = \text{MED}(|\mathbf{t} - \mathbf{1}_n \text{MED}(\mathbf{t})|), \quad (37)$$

where $\mathbf{1}_n \in \mathbb{R}^n$ denotes the vector of ones and the absolute value $|\cdot|$ is computed in a component-wise manner. In practice, we compute the depth projection function by replacing the supremum with the maximum on a finite set of elements in the hypersphere \mathbb{S}^{d-1} . Formally, the function $\rho_P : \mathbb{R}^d \rightarrow \mathbb{R}$ given by

$$\rho_P(\mathbf{x}) = \max_{\mathbf{u} \in \mathbb{U}} \frac{|\mathbf{u}^T \mathbf{x} - \text{MED}(\mathbf{u}^T \mathbf{X})|}{\text{MAD}(\mathbf{u}^T \mathbf{X})}, \quad \forall \mathbf{x} \in \mathbb{R}^d, \quad (38)$$

where $\mathbb{U} = \{\mathbf{u}_1, \mathbf{u}_2, \dots, \mathbf{u}_k\} \subset \mathbb{S}^{d-1}$, is taken as an approximation of the theoretical depth projection function ρ_P^* . The projection depth morphological approach is defined by ranking the vector-values according to the mapping $\rho_P : \mathbb{R}^d \rightarrow \mathbb{R}$ given by (38) together with a look-up table.

References

1. Angulo, J.: Morphological colour operators in totally ordered lattices based on distances: Application to image filtering, enhancement and analysis. *Computer Vision and Image Understanding* **107**(1–2), 56–73 (2007)
2. Aptoula, E., Lefèvre, S.: A Comparative Study on Multivariate Mathematical Morphology. *Pattern Recognition* **40**(11), 2914–2929 (2007)

3. Birkhoff, G.: Lattice Theory, 3 edn. American Mathematical Society, Providence (1993)
4. Burgeth, B., Didas, S., Kleefeld, A.: A Unified Approach to the Processing of Hyperspectral Images. In: B. Burgeth, A. Kleefeld, B. Naegel, N. Passat, B. Perret (eds.) *Mathematical Morphology and Its Applications to Signal and Image Processing*, pp. 202–214. Springer International Publishing, Cham (2019). DOI 10.1007/978-3-030-20867-7{_}16
5. Burgeth, B., Kleefeld, A.: An approach to color-morphology based on Einstein addition and Loewner order. *Pattern Recognition Letters* **47**(0), 29–39 (2014)
6. Chevallier, E., Angulo, J.: The Irregularity Issue of Total Orders on Metric Spaces and Its Consequences for Mathematical Morphology. *Journal of Mathematical Imaging and Vision* **54**(3), 344–357 (2016). DOI 10.1007/s10851-015-0607-7
7. Dougherty, E.R., Lotufo, R.A.: *Hands-on Morphological Image Processing*. SPIE PRESS (2003)
8. Fatras, K., Zine, Y., Flamary, R., Gribonval, R., Courty, N.: Learning with minibatch Wasserstein : asymptotic and gradient properties. In: *Proceedings of the Twenty Third International Conference on Artificial Intelligence and Statistics*, pp. 2131–2141. PMLR (2020). URL <http://proceedings.mlr.press/v108/fatras20a.html>
9. Foley, J.D., Dam, A.V., Huges, J.F., Feiner, S.K.: *Computer Graphics: Principles and Practice*, 2nd edn. Addison-Wesley, U.S.A. (1990)
10. Gonzalez, R.C., Woods, R.E.: *Digital Image Processing*, second edn. Prentice-Hall, Upper Saddle River, NJ (2002)
11. Goutsias, J., Heijmans, H.J.A.M., Sivakumar, K.: Morphological Operators for Image Sequences. *Computer vision and image understanding* **62**, 326–346 (1995)
12. van de Gronde, J., Roerdink, J.: Group-Invariant Colour Morphology Based on Frames. *IEEE Transactions on Image Processing* **23**(3), 1276–1288 (2014)
13. Haykin, S.: *Neural Networks and Learning Machines*, 3rd edn. Prentice-Hall, Upper Saddle River, NJ (2009)
14. Heijmans, H.J.A.M.: Mathematical Morphology: A Modern Approach in Image Processing Based on Algebra and Geometry. *SIAM Review* **37**(1), 1–36 (1995)
15. Levkowitz, H.: *Color Theory and Modeling for Computer Graphics, Visualization, and Multimedia Applications*. Kluwer Academic Publishers, Norwell, Massachusetts, USA (1997)
16. Levkowitz, H., Herman, G.T.: GLHS: A Generalized Lightness, Hue, and Saturation Color Model. *CVGIP: Graphical Models and Image Processing* **55**(4), 271–285 (1993). DOI 10.1006/cgip.1993.1019
17. Lézoray, O.: Complete lattice learning for multivariate mathematical morphology. *Journal of Visual Communication and Image Representation* **35**, 220–235 (2016). DOI 10.1016/j.jvcir.2015.12.017
18. Najman, L., Talbot, H. (eds.): *Mathematical Morphology: From Theory to Applications*. John Wiley & Sons, Inc., Hoboken, NJ, USA (2013). DOI 10.1002/9781118600788
19. Peyré, G., Cuturi, M.: Computational optimal transport. *Foundations and Trends in Machine Learning* **11**(5-6), 1–257 (2019). DOI 10.1561/22000000073. URL <http://dx.doi.org/10.1561/22000000073>
20. Pitié, F.: Advances in colour transfer. *IET Computer Vision* **14**(6), 304–322 (2020). DOI 10.1049/iet-cvi.2019.0920. URL www.ietdl.org
21. Pitié, F., Kokaram, A.C., Dahyot, R.: N-dimensional probability density function transfer and its application to colour transfer. In: *Proceedings of the IEEE International Conference on Computer Vision*, vol. II, pp. 1434–1439 (2005). DOI 10.1109/ICCV.2005.166
22. Ronse, C.: Why Mathematical Morphology Needs Complete Lattices. *Signal Processing* **21**(2), 129–154 (1990)
23. Rubner, Y., Tomasi, C., Guibas, L.J.: Earth mover’s distance as a metric for image retrieval. *International Journal of Computer Vision* **40**(2), 99–121 (2000). DOI 10.1023/A:1026543900054. URL <https://link.springer.com/article/10.1023/A:1026543900054>
24. Sangalli, M., Valle, M.E.: Color Mathematical Morphology Using a Fuzzy Color-Based Supervised Ordering. In: G.A. Barreto, R. Coelho (eds.) *Fuzzy Information Processing*, pp. 278–289. Springer International Publishing (2018)
25. Sangalli, M., Valle, M.E.: Approaches to Multivalued Mathematical Morphology Based on Uncertain Reduced Orderings. In: B. Burgeth, A. Kleefeld, B. Naegel, N. Passat, B. Perret (eds.) *Mathematical Morphology and Its Applications to Signal and Image Processing*, pp. 228–240. Springer International Publishing, Cham (2019). DOI 10.1007/978-3-030-20867-7{_}18
26. Schmitzer, B.: Stabilized sparse scaling algorithms for entropy regularized transport problems. *SIAM Journal on Scientific Computing* **41**(3), A1443–A1481 (2019). DOI 10.1137/16M1106018. URL <http://www.siam.org/journals/sisc/41-3/M110601.html>
27. Schölkopf, B., Smola, A.: *Learning with Kernels: Support Vector Machines, Regularization, Optimization, and Beyond*. MIT Press, Cambridge, MA (2002)

28. Serra, J.: The “False Colour” Problem. In: M.H.F. Wilkinson, J.B.T.M. Roerdink (eds.) *Mathematical Morphology and Its Application to Signal and Image Processing, Lecture Notes in Computer Science*, vol. 5720, pp. 13–23. Springer Berlin Heidelberg (2009)
29. Soille, P.: *Morphological Image Analysis*. Springer Verlag, Berlin (1999)
30. Valle, M.E., Francisco, S., Granero, M.A., Velasco-Forero, S.: Measuring the Irregularity of Vector-Valued Morphological Operators Using Wasserstein Metric. In: Lindblad J., Malmberg F., Sladoje N. (eds) *Discrete Geometry and Mathematical Morphology. DGMM 2021. Lecture Notes in Computer Science*, vol. 12708, pp. 512–524. Springer, Cham (2021). DOI 10.1007/978-3-030-76657-3{_}37
31. Valle, M.E., Valente, R.A.: Mathematical Morphology on the Spherical CIELab Quantale with an Application in Color Image Boundary Detection. *Journal of Mathematical Imaging and Vision* **57**(2), 183–201 (2017). DOI 10.1007/s10851-016-0674-4. URL <https://link.springer.com/article/10.1007/s10851-016-0674-4>
32. Vapnik, V.N.: *Statistical Learning Theory*. John Wiley and Sons, New York, NY, USA (1998)
33. Velasco-Forero, S., Angulo, J.: Mathematical Morphology for Vector Images Using Statistical Depth. In: P. Soille, M. Pesaresi, G.K. Ouzounis (eds.) *Mathematical Morphology and Its Applications to Image and Signal Processing*, pp. 355–366. Springer Berlin Heidelberg, Berlin, Heidelberg (2011)
34. Velasco-Forero, S., Angulo, J.: Supervised Ordering in \mathbb{R}^p : Application to Morphological Processing of Hyperspectral Images. *IEEE Transactions on Image Processing* **20**(11), 3301–3308 (2011). DOI 10.1109/TIP.2011.2144611
35. Velasco-Forero, S., Angulo, J.: Random Projection Depth for Multivariate Mathematical Morphology. *IEEE Journal of Selected Topics in Signal Processing* **6**(7), 753–763 (2012). DOI 10.1109/JSTSP.2012.2211336
36. Velasco-Forero, S., Angulo, J.: Vector Ordering and Multispectral Morphological Image Processing. In: M.E. Celebi, B. Smolka (eds.) *Advances in Low-Level Color Image Processing*, pp. 223–239. Springer Netherlands, Dordrecht (2014). DOI 10.1007/978-94-007-7584-8{_}7
37. Villani, C.: *Optimal Transport, Grundlehren der mathematischen Wissenschaften*, vol. 338. Springer Berlin Heidelberg, Berlin, Heidelberg (2009). DOI 10.1007/978-3-540-71050-9. URL <http://link.springer.com/10.1007/978-3-540-71050-9>